FASR Flare Science: Lessons from the Nobeyama Radioheliograph

Dale E. Gary
Center for Solar-Terrestrial Research, New Jersey Institute of Technology
323 M L King Blvd, Newark, NJ 07102
dgary@njit.edu

Abstract

We compare and contrast the instrumental parameters of the Nobeyama Radioheliograph (NoRH) and the future Frequency Agile Solar Radiotelescope (FASR) with an emphasis on flare research. The primary results and discoveries of NoRH in the realm of flare science are presented and used to motivate many of the choices for design parameters and science goals for FASR. Key parameters of NoRH for flare science are its dual-frequency, dual-polarization, excellent image quality, solar-dedicated and solar-optimized design, and high time resolution. Its main limitations are spatial resolution, frequency coverage, and frequency resolution. FASR's design makes use of the strengths of NoRH, and adds these three missing elements: a factor of 10 improvement in spatial resolution, broad frequency coverage and high frequency resolution. We discuss the manner in which these improvements extend the legacy of NoRH for flare science.

Key words: Sun:flares Sun:corona radio:instrumentation

1. Introduction

The Nobeyama Radioheliograph (NoRH, Nakajima et al. 1994) has now operated over more than a solar activity cycle, and has amassed the largest database to date of solar flare radio imaging data. This paper reviews some of the major discoveries and lessons learned from this large database, and the studies done by an international community of researchers over the 13 years from 1992-2004, in order to apply them as we plan for a new radio facility, the Frequency Agile Solar Radiotelescope (FASR).

Radio studies of the Sun are well known to provide unique information unavailable by any other means. Chief among the unique aspects is (1) sensitivity to magnetic field strength, but also important are (2) direct information on the coronal component of the high energy electron population, (3) simultaneous sensitivity to the thermal and nonthermal electron populations, (4) the fact that the emission may be both optically thick and optically thin in different parts of the radio spectrum, and (5) the sensitivity to coherent emission, which renders even a relatively small number of electrons visible.

These advantages, when combined with observations at other wavelengths, help to provide a full picture of the solar atmosphere and activity therein. For flare research, radio emission is most complementary with soft and hard X-ray observations, which are sensitive to the same electrons, but with different weighting. The hard X-rays are generally from loop footpoints, where the electrons meet the chromosphere, while the radio emission provides information about the coronal population. The soft X-rays provide mostly thermal plasma diagnostics, and are entirely optically thin, whereas the radio emission provides both thermal and nonthermal diagnostics and may be both optically thick and thin at different radio frequencies. The radio emission is complementary to Hα, EUV and white-light coronagraph observations in the case of wave and eruptive phenomena (filaments, prominences, CMEs). For non-flare research, the radio observations are highly complementary to magnetographs, chromospheric and coronal observations in the optical, UV, EUV and soft X-rays.

The two NoRH frequencies, 17 and 34 GHz, are often optically thin and well above frequencies where the coronal plasma typically supports coherent emission. Therefore, the results from Nobeyama mainly involve advantages 1–3 from the list above, although advantage 4 is sometimes made use of. To make full use of the entire list, however, requires broad frequency coverage, which is what FASR is designed to do. As we will see, FASR takes many design parameters from Nobeyama, such as the use of many small antennas for excellent imaging with full-Sun coverage, high time resolution, solar-dedicated and solor-optimized design, and pipelined data processing to remove the burden of image reconstruction from the typical user.

In § 2 we list the basic parameters and main science goals of FASR. In § 3 we first list the instrumental parameters of NoRH that are important for flare research, and then examine some of the main discoveries and results of NoRH for flare science. In § 4 we compare and constrast the instrumental parameters of FASR and NoRH, and discuss how FASR can be expected to extend the NoRH legacy for flare science. Finally, we conclude in § 5.

2. The Frequency Agile Solar Radiotelescope

The broad outlines of the FASR instrument have been described in numerous publications (e.g. Bastian 2003*ab*; Gary 2003; Gary & Keller 2003; White et al. 2003), while much of the science is presented in Gary & Keller (2004). Here we briefly describe the FASR instrument concept in order to examine the similarities and differences with the

Fig. 1. Artist's conception of the FASR-A and FASR-B arrays on the Plains of San Augustine.

NoRH. The nominal frequency range of FASR covers three orders of magnitude, from roughly 30 MHz to 30 GHz. No single antenna and feed system can cover so great a range in frequency, so the design calls for three separate systems, which we designate FASR-A (covering 2-30 GHz), FASR-B (covering 200-3000 MHz), and FASR-C (covering 30-300 MHz). Each array will have a maximum baseline of 6 km, providing spatial resolution of $20''/f_{\rm GHz}$ at 30° elevation, where $f_{\rm GHz}$ is the frequency in GHz. Table 1 gives some general characteristics of the three arrays. An artist's conception of the FASR-A,B arrays is shown in Figure 1. In order to accomplish the broad range of science envisioned, the FASR receivers and digital signal processing requires the capabilities listed in Table 2.

Table 1. Characteristics of FASR's Three Arrays

Array Designation	Number Antennas	Frequency Range	Antenna Size/Type
FASR-A high ν array	~ 100	2-30 GHz	2 m
FASR-B low ν array	~ 60	0.2-3 GHz	6 m
FASR-C dipole array	~ 40	30-300 MHz	log dipoles

Table 2. FASR Receiver Specifications

Quantity	Spec
Frequency Resolution	0.1% (FASR-C)
	1% (FASR-A,B
Time Resolution	10 ms (FASR-B,C)
	100 ms (FASR-A
Polarization	Stokes IV (QU)
Instantaneous Bandwidth	~ 1 GHz

FASR will have to calibrate for instrumental/environmental changes such as temperature and other secular changes, as well as external variations such as the troposphere (weather) above ~ 1 GHz and the ionosphere below that frequency. The design will emphasize instrumental stability and monitoring of secular changes (including a front-end noise cal source and phase monitoring), so that cosmic sources may be used only before sunrise and after sunset for absolute amplitude and phase calibration. During solar observations, self-calibration methods will be used for the FASR-A,B arrays, and monitoring of ionospheric tip-tilt will be done, perhaps through the use of GPS measurements of total electron content, for the FASR-B,C array.

FASR will be designed to be the world's premier solar radio facility for at least two decades after completion. The science goals include:

- Directly measure coronal magnetic fields
- Image coronal mass ejections (CMEs)
- Obtain radio spectral diagnostics of particle acceleration and energy release, with excellent spatial and temporal resolution
- Image radio emission from shocks (type II), electron beams (type III), and other bursts over heights 1-2.5 $R_\odot$
- Construct 3D solar atmospheric structure (T, B, n_e) over a wide range of heights

The science to be addressed in each of these areas, and some of the challenges for FASR, were raised at an international science workshop held 2002 May in Green Bank, WV, and at a special session of the American Astronomical Society in 2002 June. The topics presented at these two meetings were expanded and collected in a book in the Kluwer *Astronomy and Astrophysics Library* series (Gary & Keller 2004). For the purposes of this paper, we emphasize flare science (energy release, particle acceleration, and related activity), and the legacy of NoRH for our current understanding of these phenomena.

3. Nobeyama Legacy for Flare Science

The instrumental parameters of NoRH that are relevant to flare science are:

- dual frequency operation at 17 and 34 GHz, both of which are typically optically thin and provide sensitivity to both thermal and nonthermal emission
- full Sun field of view, which insures that no event or phenomenon on the visible disk is missed
- solar-dedicated operation and solar-optimized performance, which provides coverage and optimal data quality on every event or phenomenon
- dual circular polarization, which is critical to the interpretation of the emission for physical diagnostics
- spatial resolution of $15''$ (17 GHz) and $8''$ (34 GHz)
- uses the Sun itself for calibration, based on redundant baselines and the fact that the solar disk brightness at 17 and 34 GHz is relatively constant
- 84 antennas (providing > 1500 independent baselines) for excellent imaging properties

- pipeline processing scheme for quick look and permanent archiving of images
- 50 ms time resolution, with 1 s resolution for non-flare data

The strengths and limitations contained in the above list of properties color the results that we will examine in this section. The results detailed below make it clear which properties should be emulated by FASR and which should be improved upon. Thus, the results from NoRH are a treasure to be exploited fully in the design of FASR. Of course, many new results are still to come from the NoRH, both from new observations and from new studies of the events already contained in the NoRH database. It is important that the NoRH continue to operate, and the FASR design continue to be examined in the light of these continued new discoveries.

3.1. Source Morphology

The NoRH spatial resolution is often not sufficient to fully resolve individual burst sources, but Hanaoka (1997) was able to deduce the morphology of small loops, with closely spaced footpoints, by examining their polarization signature. Figure 2 illustrates this. What appears to be two well-separated sources in Stokes I (Fig. 2*e*) is revealed from the polarization (V/I) image (Fig. 2*f*) to be three separate footpoints as shown schematically in Fig. 2*i*. This conclusion can be checked by referring to such other data as the Yohkoh SXT image in Fig. 2*h*.

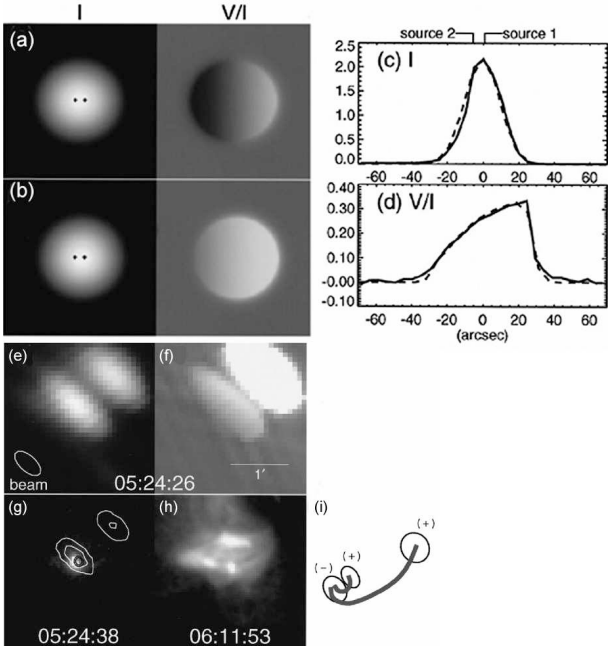

Fig. 2. Using polarization as a guide to morphology (from Hanaoka 1997).

Using similar methods, Nishio et al. (1997; 2000) studied 25 events at 17 GHz, selected for relatively simple time profiles (single, or multiple but well separated, spikes

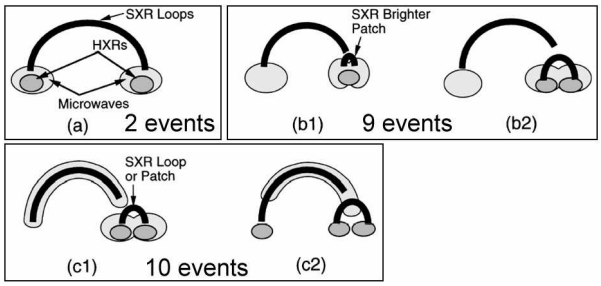

Fig. 3. Schematic diagram of flare morphological types based on 17 GHz microwave (NoRH), and HXR (HXT) observations (from Nishio et al. 1997).

with durations of order 10 s), to obtain statistics of occurrence for different morphological classes. The descriptive types included not only the radio morphology but also the accompanying soft X-ray (SXR) and hard X-ray (HXR) morphology seen with Yohkoh SXT and HXT. The results are summarized in Figure 3, from Nishio et al. (1997) who defined 3 basic types, two of which are divided into two subclasses each. The types are stated as follows:

- cospatial microwave/HXR double sources (type *a*)
- double microwave source with a single HXR source on one side (type *b*1)
- double microwave source with a double HXR source on one side (type *b*2)
- single, elongated microwave source with a double HXR source on one side (type *c*1)
- single, elongated microwave source with three HXR sources (double on one side, and a remote one connected by the loop on the other side) (type *c*2)

Among the list of 25 events described by Nishio et al. (2000), Fig. 3 indicates the number of events of type *a* (2 events), *b* (9 events), and *c* (10 events). A minority of bursts (4) were denoted unclassified (type *u*) because their morphology fit none of the above descriptions. From this study and others (e.g. Kundu et al. 1995; Hanaoka 1997), we can conclude that most bursts show some asymmetry at 17 GHz. The microwave emission may come from either the looptop, or the footpoints, or both. Missing from this list are events showing almost no spatial structure (even with super-resolution using a 5″ restoring beam), such as the 5 events reported by Kundu et al. (2001*c*).

It is clear from the NoRH morphological studies that FASR's factor of 10 higher spatial resolution will be needed.

3.2. Dual Frequency Loop Observations

A subset of the type *c* events are those for which the microwave source is not only elongated, but shows a clear loop shape. Those that have been studied at both 17 and 34 GHz are especially useful for comparison with theoretical expectations. In this section we discuss some of these observations and some important implications for the accelerated electron energy and pitch angle distributions. It should be kept in mind, however, that the events discussed

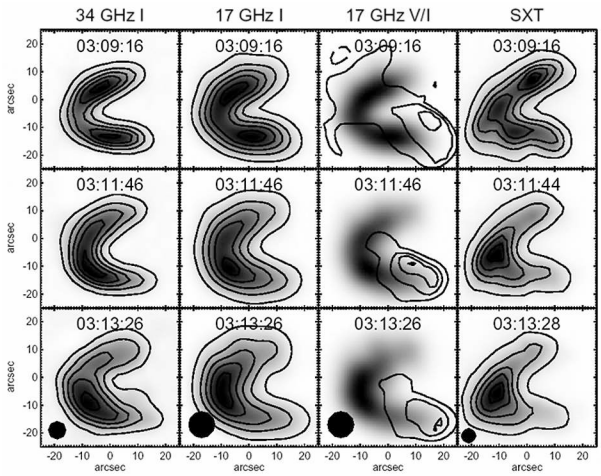

Fig. 4. Dual-frequency loop observations at different times for the event of 1999 May 29, near 03:10 UT. Shown are images at 34 GHz (left column), 17 GHz Stokes I (second column), 17 GHz Stokes V (third column), and soft X-rays (right column). (From White et al. 2002).

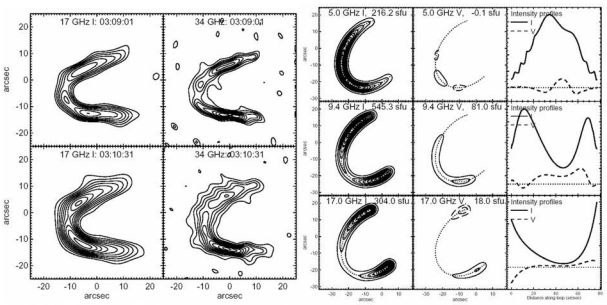

Fig. 5. 17 and 34 GHz NoRH images at two selected times deconvolved using 0.5″ pixels and a maximum entropy algorithm. These are the model brightness distributions resulting from the deconvolution; i.e., they have not been smoothed with a Gaussian in the way that the images in Fig. 4 were.

here are rather rare, being large (40-80″ long), and loop-shaped (i.e. not footpoint) sources. Higher resolution is needed to determine whether the conclusions drawn from these events also pertain to the more typical small loops discussed above.

A rather complete study of such a loop event was done by White et al. (2002), as shown in Figure 4. The appearance of the loop at 34 and 17 GHz are shown in the first two columns at various times during its development. The source is also loop-like as seen in soft X-rays (last column, from SXT), while the HXT sources (not shown) were footpoint sources in M1, M2 and H channels (i.e. > 23 keV energies). Note that the radio emission early on (at 03:09 UT) is concentrated near the footpoints, but part way up the loop legs. Later the source peaks more or less at the loop top.

The left four panels of Figure 5 show the same observations at two times, reconstructed with a maximum entropy algorithm but not convolved with a gaussian restoring beam. The panels on the right show a typical flaring loop model, for electrons with isotropic pitch angles, for comparison with images at three microwave frequencies and brightness and polarization profiles (far right column) along the loop axes. There is a clear tendency for the high-frequency (> 17 GHz) emission in the model to be concentrated at the footpoints, in clear disagreement with the observations. White et al. (2002) point out the need for a mechanism to keep the electrons concentrated near the loop top.

Melnikov et al. (2002*a*) did a comparative analysis of four such loop sources, for which the brightness profiles along the loop axes at the time of peak flux density are shown in Figure 6. In each case, the 17 and 34 GHz emission is concentrated at or near the loop tops, again in violation of expectations from simple loop models.

Melnikov et al. (2002*a*) examined the range of param-

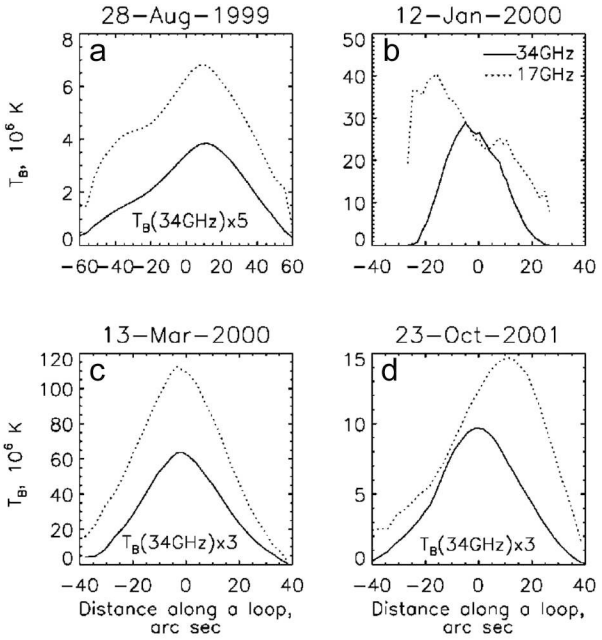

Fig. 6. Spatial distribution of radio brightness temperatures at 34 GHz (solid line) and 17 GHz (dotted line) along a flaring loop for the four events under study. (From Melnikov et al. 2002*a*).

eter values that would be necessary to form a loop-top source, as shown in Figure 7, for a model loop with modest mirror ratio $B_{\rm tr}/B_0 = 2$, where $B_{\rm tr}$ is the magnetic field strength in the transition region (the base of the loop), and B_0 is the field strength at the loop top. They found that a significant pitch angle anisotropy is needed. An isotropic pitch angle distribution (panel b) concentrates the electrons near the loop top, but when the emission is calculated (panel e) the dependence of emissivity on magnetic field strength causes the emission to peak near the footpoints of the loop. Among the models considered by Melnikov et al. (2002a), the emission is concentrated near the loop top only for a pancake pitch angle distribution:

$$\phi(\mu_0) = \exp[-(1-\mu_0)^2/\mu_1^2],$$

where $\mu_0 = \cos\alpha$ (α is the pitch angle), and μ_1 is a constant parameter describing the width of the distribution (Fig. 7f). For Fig. 7c, f, the electrons are quite well constrained to pitch angles perpendicular to the magnetic field ($\mu_1 = 0.4$), which says something important about the acceleration mechanism. Other evidence by Lee, Gary & Shibasaki (2000), described in §3.3, agrees with the idea that electrons are accelerated at least initially with pitch angles in a pancake distribution.

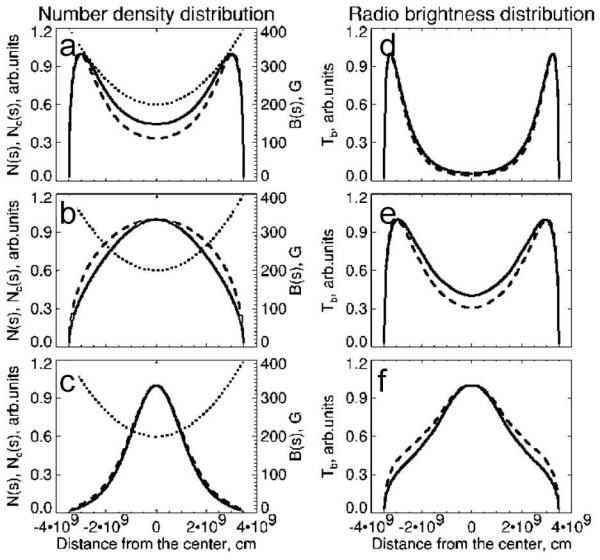

Fig. 7. Normalized spatial distributions along a loop. *Left panels:* Number density (dashed line) and column number density (solid line) for the (a) beamlike, (b) isotropic, and (c) pancake electron pitch-angle distributions; the magnetic field distribution is shown as a dotted line, the mirror ratio $B_{\rm tr}/B_0 = 2$, and the loss-cone pitch angle $\alpha_l = 45°$. *Right panels:* Corresponding gyrosynchrotron intensity in the optically thin regime (at 34 GHz). (From Melnikov et al. 2002a).

Some general conclusions can be deduced from dual-frequency loop observations and models:

- About half of the "large" loop events observed at 17 and 34 GHz are brighter near the footpoints, as expected from earlier models.

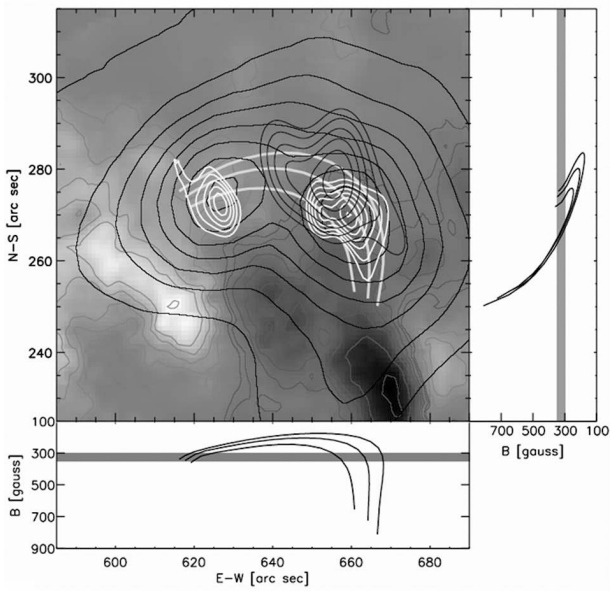

Fig. 8. Radio morphology and magnetic fields at the impulsive phase of a flare. The center frame shows 5 GHz (thick black contours), 10.6 GHz (white contours) and 17 GHz (thin black contours) on top of the longitudinal magnetogram. The thick white curves are selected field lines from the field extrapolation to represent the loop involved with the flare. Two boxes at the right and bottom give the field strength of the three field lines as function of distance along east-west and north-south, respectively. The gray strips in the boxes are to locate the magnetic trap (from Lee et al. 2000).

- However, a significant number have looptop sources, an observation that appears to require anisotropic pitch angles for the injected electrons.
- We must be more sophisticated in our models to account for even the grossest of characteristics for some events, i.e. the concentration of radio brightness at the top of loops.

The higher spatial resolution and much greater frequency coverage of FASR will give more complete loop diagnostics, as well as allowing smaller loops to be studied. We are sure to find that the simple models that assume isotropic pitch angle distributions will have to be thrown out. However, we can expect to discover new clues to the nature of the energy release and particle acceleration through studying the pitch angle distribution.

3.3. Electron Dynamics

In addition to the spatial morphology of radio sources, NoRH has provided excellent data of the dynamical development of the radio emission (e.g. Melnikov et al. 2002b). Lee et al. (2000) used the morphology of the bursts at several frequencies (17 GHz from NoRH, and 5.0 and 10.6 GHz using OVSA) to identify the magnetic topology of the flaring loop. This was compared to magnetic field extrapolations to estimate the magnetic field strength in the radio sources, to identify mirror points of the electrons, as shown in Figure 8.

The specific geometry obtained from Fig. 8 allowed a

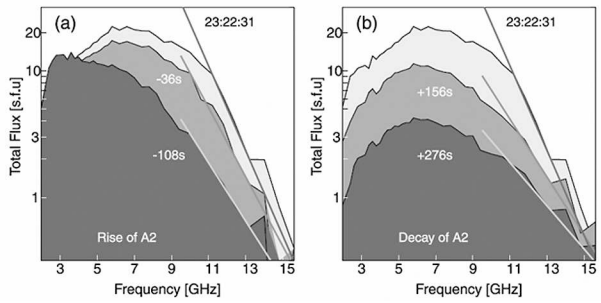

Fig. 9. Spectral variation of the event in Fig. 8: (*a*) and (*b*) show total power spectra in the rise and decay phase, respectively, at five selected times relative to the time of the maximum flux. The straight lines are guide lines for spectral slope at the corresponding times (from Lee et al. 2000).

rather complete magnetic loop model to be developed, in which accelerated electrons of different energy and pitch angles were introduced in an attempt to match the spectral dynamics shown in Figure 9. In order to match the changes in spectral slope, and at the same time the relative flux densities on the optically thin side of the spectrum, the pitch angle distribution had to be restricted to a pancake distribution that was initially narrow (small μ_1 in the notation above) but broadened over time due to collisions.

As a result of the flare morphologies mentioned in § 3.1, the footpoint source at the remote end of the longer loop may show "time-of-flight" (TOF) delays in radio and/or hard X-rays (e.g. Bastian 1999). Hanaoka (1999) studied three such events, using the high time resolution (50 ms) capability of NoRH. Results for one of the events are shown in Figure 10. There is a clear indication that the radio emission from the remote source is delayed about 500 ms relative to the emissions from the main source. The delay in this and the other two flares indicates a velocity for the exciter of about $0.5c$, suggesting that the exciter is high-energy electrons that are accelerated first in the vicinity of the main source and then arrive in the remote source.

It should be mentioned that other exciters and propagation speeds have been seen in other events. Yokoyama et al. (2002), again using the high-time-resolution NoRH data, imaged a traveling disturbance in a radio loop moving with a speed of 6×10^3 km s^{-1}, consistent with the Alfven velocity in the loop. We note that FASR will likewise be able to follow such fast dynamics, but will have the advantage of images at many frequencies. This will allow the electrons to be followed along the loop as their emitting frequency shifts due to the changing magnetic field. Such observations will yield a more complete picture of the transport of electrons, and will also allow deduction of the magnetic field strength within the loop along which the electrons are propagating.

3.4. Long Duration Events

In addition to the rather short-lived impulsive events described in the foregoing, NoRH has provided detailed

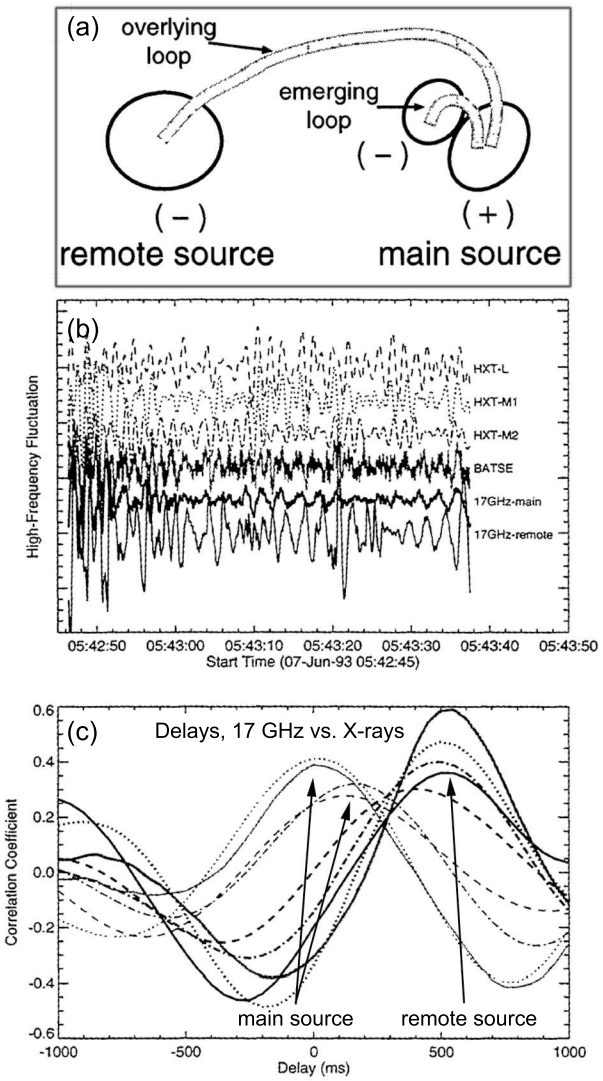

Fig. 10. *a*) Schematic drawing of the loop geometry of the event of 1993 June 07. *b*) Rapidly fluctuating components filtered from the HXR and NoRH spatially resolved light curves. *c*) cross-correlations between time profiles in *b*. Curves representing the main component all occur within 200 ms of each other, while the HXR curves and the 17 GHz main source occur more than 500 ms before the 17 GHz remote source (adapted from Hanaoka 1999).

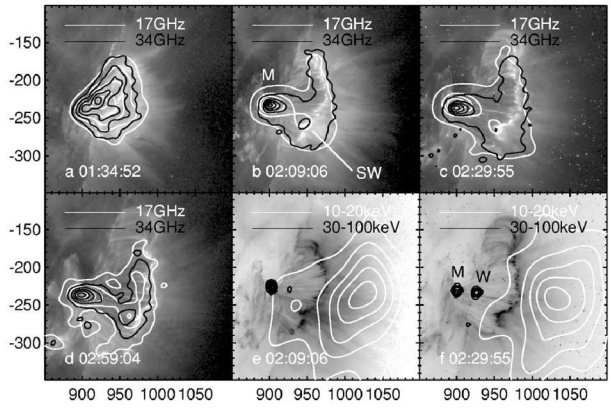

Fig. 11. Evolution of the radio and hard X-ray sources later in the flare of 2002 Apr 21. The first four images show a sequence of overlays of 17 (white contours) and 34 (black contours) GHz images on TRACE 195 Å Fe XII images during the extended phase of the flare when the loop system is expanding above the west limb. The last two images show contours of the RHESSI 1020 keV (white) and 30 100 keV (black) emission overlaid on the TRACE 195 Å Fe XII images at 02:09:56 and 02:29:55 (displayed with inverted color table) (from Kundu et al. 2004).

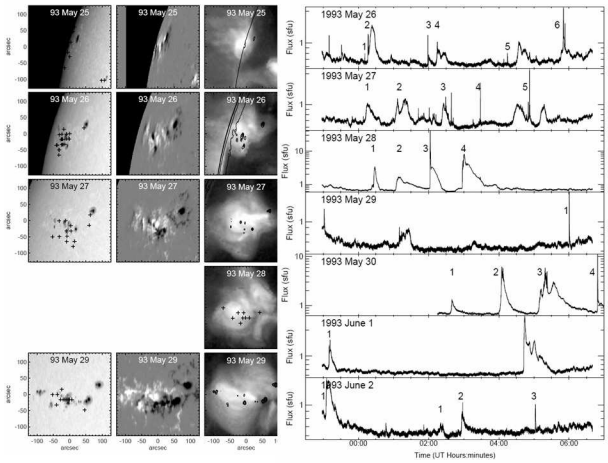

Fig. 12. *Left Side:* Sequence of white-light images (left), KPNO magnetograms (second column), and Yohkoh SXT images (third column) for the period 1993 May 25 to May 29 (there are no KPNO data for May 28). The plus signs on the white-light images represent the locations of optical flares, while contours of the white-light images are overplotted on the soft X-ray images to show the locations of sunspots. *Right Side:* Time profiles of the bursts observed by NoRH at 17 GHz during the period 1993 May 26 to June 3. (From Kundu et al. 2001*b*).

observations of the morphology and evolution of long duration events, which are typically associated with two-ribbon flares and the development of post-flare loop systems.

An example of a well-observed event is the one studied by Kundu et al. (2004), which also happens to be the first large (X-class) flare that RHESSI observed. Images from later in the event are shown in Figure 11, and clearly show the correspondence of the radio emission with the post-flare loops seen in TRACE. Kundu et al. (2004) conclude that this flare is striking in the complex and numerous ways that radio emission could be generated within multiple acceleration sites over a long period of time. Another example of a long-duration event observed with NoRH is that reported by Altyntsev et al. (1999). Again, this event showed a close correspondence with post-flare loops being formed at the closing of once open fields in the classic two-ribbon flare scenario. FASR will improve on these results due to its higher spatial resolution, but also due to its broad frequency coverage, which will allow more complete diagnostics of the conditions both in the flaring loops and in the region above the loops. We come back to this in § 4.3.

3.5. Flare Productivity and Space Weather

Because of the large database of radio bursts available from the NoRH, and its solar-dedicated operation, statistical studies of flare productivity are possible (Kundu et al. 2001*b*). In addition, although high-frequency radio emission at 17 and 34 GHz is not optimum for studies of space weather (that is, studies of the influence of solar activity on the Earth and near-Earth environment), NoRH data have proven useful for such space-weather-related phenomena as coronal heating (White et al. 1995), eruptive events (Hori et al. 2000), and connecting near-surface phenomena to metric burst (type II and III) activity (Nakajima & Yokoyama 2002; Aurass et al. 2002).

Kundu et al. (2001*b*) examined dozens of bursts that occurred at 17 GHz in a single active region over 9 days in May/June 1993, to study the evolution in spatial structure of the region in relation to flare activity. Despite its being a rather complex active region, the region had only weak, but repetitive flaring at 17 GHz (see Figure 12), leading the authors to suggest that many small events in a "typical" active region may be a sign of relaxation of energy buildup, avoiding major flares.

Figure 13, also from Kundu et al. (2001*b*), compares the spatial structure for 16 weak bursts (gray scale background) with the quiet active region emission (contours). No clear pattern is discernible, but more information is needed than is provided by images at a single radio frequency. Through its spectral diagnostics, FASR will provide magnetic field and temperature maps of the active region, along with full spectroscopic imaging of the events (and at 10 times higher spatial resolution). Radio diagnostics should allow us to track energy release and conversion to heating.

In related work, White et al. (1995) investigated the 17 GHz radio counterparts of small brightenings seen in soft X-rays, which at that time were referred to as active region transient brightenings, but have since been identified (Gary, Hartl & Shimizu 1997) with the microflares first reported by Lin et al. (1984). White et al. (1995) could not distinguish the bursts at 17 GHz from thermal heating events, but Gary, Hartl & Shimizu (1997), using OVSA observations ranging from 1–18 GHz in frequency,

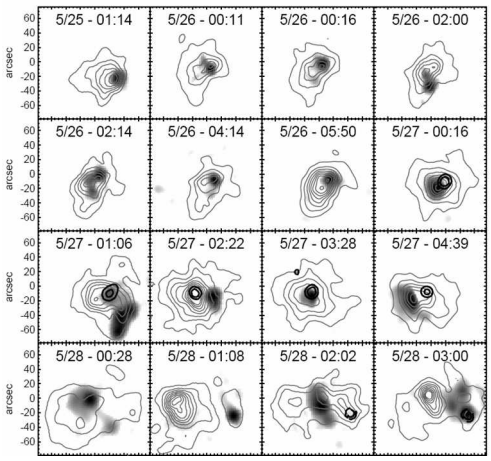

Fig. 13. Preflare active region emission contours (gray) from 15,000–120,000 K overlaid on a gray-scale representation of the subsequent burst emission for 16 flares. Black contours show strong circular polarization in the preflare maps (from Kundu et al. 2001*b*).

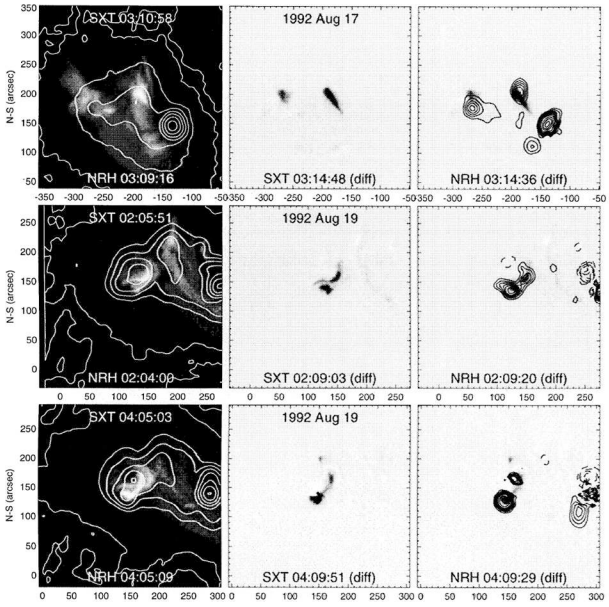

Fig. 14. Four active region transient brightenings (from White et al. 1995). *Left Column:* quiet active region emission just before the outburst, *Middle:* SXT difference image showing the soft X-ray transient, *Right:* NoRH 17 GHz difference image (contours) overlaid on the SXT difference image.

were able to identify copious nonthermal emission, with all of the characteristics of ordinary flares, only with energy output of order $< 10^{29}$ ergs. Since then, even smaller radio events have been seen (Krucker et al. 1997), both in and out of active regions. FASR should be extremely sensitive to small events, primarily due to its wide spectral coverage. The OVSA results showed that the spectral characteristics can vary widely, and FASR's excellent imaging will pick up a burst no matter what its peak frequency may be.

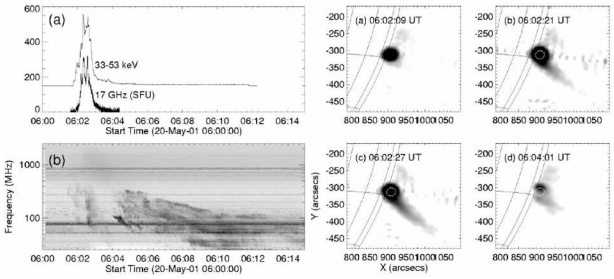

Fig. 15. *a*) Time profile of a burst at 17 GHz and 33–53 keV hard X-rays. *b*) Associated Hiraiso dynamic spectrum showing a type II and type III burst. *Right panels:* NoRH 17 GHz radio images showing the development of a collimated ejector during the burst. (From Nakajima & Yokoyama 2002).

Despite the fact that NoRH operates at high microwave frequencies for which typically only near-surface phenomena are visible, in many events there is a hint of a connection with much larger-scale phenomena. The event shown in Figure 15, for example, seems to show a connection between the main phase of the flare and large scale loops extending upward from it, and possibly a connection with the associated type III burst. Likewise, Aurass et al. (2002) studied two events seen with NoRH that had accompanying type II bursts, and were able to relate moving features at 17 GHz (which they referred to as "type II burst-exciting disturbances") with EIT waves and, temporally, with features seen in the dynamic spectrum from Potsdam. We discuss in the next section FASR's expected performance in relating the low-atmosphere phenomena with large-scale features.

4. Lessons Learned

In this section we discuss specific lessons from NoRH and other existing instruments that have gone into our current design for FASR. We also outline the ways in which FASR can be expected to extend the flare science of NoRH.

4.1. FASR Instrumental Parameters and the NoRH Legacy

Refering to § 2, we can see how the FASR design makes use of the lessons learned from the NoRH results of § 4. Like NoRH, the FASR design incorporates full-Sun coverage to as high a frequency as possible (17 GHz for 2 m antennas), solar-dedicated operation and solar-optimized design. This will allow FASR to observe every solar burst that occurs during its observing day, with instrumental characteristics that are optimized for the spatial, spectral, and temporal variability (and dynamic range) presented by the Sun. Taking another lesson from NoRH, FASR also employs a large number of antennas, and hence a large number of baselines (~ 5000) for excellent imaging and dynamic range.

FASR also incorporates NoRH's high time resolution (10-100 ms in the case of FASR) in order to follow the

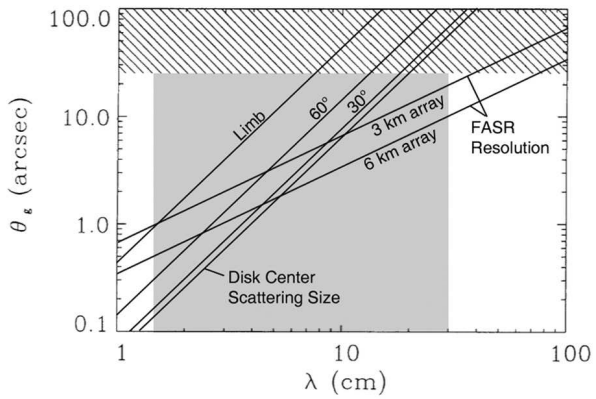

Fig. 16. Spatial resolution as a function of wavelength, showing coronal scattering limits (steep diagonal lines) for different distances from disk center—Limb, 60°, 30° and Disk Center—and the FASR resolution for arrays both 3 and 6 km maximum baseline. The FASR frequency range is shown as the gray rectangle. (Adapted from Bastian 1994).

dynamical behavior inherent in impulsive solar bursts, including delays due to time of flight. A challenge for FASR will be to cover a large range of frequency at the relevant timescales. With an instantaneous bandwidth of 1 GHz, FASR will require many sample times to cover the ~ 30 GHz total bandwidth. Therefore, observing modes will have to be developed that allow the instrument to follow the most "interesting" spectral range of the burst at high time resolution while providing wider spectral coverage at lower time resolution.

The NoRH instrumental limitations, too, inform the design of FASR. For example, the spatial resolution of NoRH is clearly insufficient to provide the detail needed resolve most sources and to follow spectral and spatial evolution. Therefore, the 6 km maximum baselines of FASR, about 10 times longer than those of NoRH, are chosen to give FASR a spatial resolution of at least $20''/\nu_{\rm GHz}$ for Sun elevations of greater than 30°. This spatial resolution compares well with the fundamental limitation on source size given by typical coronal scattering (Bastian 1994), as shown in Figure 16. FASR resolution is better than the scattering limit at wavelengths longer than 5 cm (6 GHz) over the entire disk, and over 3/4 of the disk to 2.3 cm (13 GHz).

Likewise, the dual-frequency operation of NoRH is often too restrictive to provide adequate, unambiguous diagnostics of the source and electron parameters, and the relatively high frequencies (17 and 34 GHz) restrict sources to relatively low heights, high densities (for thermal emission) and high magnetic field strength (for gyroemission). FASR's three decades of frequency coverage are chosen to enable it to observe phenomena throughout the Sun's atmosphere from the low chromosphere to a height of roughly $2.5R_\odot$, and will make it sensitive to radio emission from virtually any solar radiation mechanism. Meanwhile, its frequency resolution will enable spectral diagnostics (e.g. Gary & Hurford 2004) for measuring coronal magnetic fields, densities and temperatures, as well as a variety of high-energy electron parameters.

4.2. The Challenge of High Spatial Resolution

The combination of high spatial resolution and full-Sun coverage is a significant challenge for FASR at the higher end of its frequency range (at > 10 GHz). A comparison with NoRH is enlightening. Consider the number of independent measurements by NoRH (1500 baselines of amplitude and phase, i.e. 3000 independent measurements) and the number of resolution elements on the full disk of the Sun at 17 GHz (about $[d_\odot/d_{\rm beam}]^2 = [1920''/15'']^2 \approx 16000$). A reasonable figure of merit for imaging performance would be the ratio of these, or $3000/16000 \approx 0.19$. FASR will have a somewhat larger number of baselines, providing ~ 10000 independent measurements, but a far smaller beam ($1.17''$ at 17 GHz), giving a value for this figure of merit $10000/2.7 \times 10^6 \approx 0.0037$—more than 1400 times worse. However, there are several problems with this naive argument that make the situation for FASR far less dire than it may appear.

First, one does not need to fully characterize every resolution element on the Sun, only those containing the bulk of the flux density. Put another way, if we consider the chromosphere to be a uniform brightness temperature on which is superimposed a finite number of sources of higher and lower brightness temperature, then in a single-frequency snapshot image FASR will be able to characterize some 1700 sources (assuming "characterize" means to determine 2D position (x, y), major and minor axes (a, b), orientation, and brightness). By the same argument, NoRH can characterize 500 such sources. Although we cannot be sure at present how many sources are "enough" to characterize the entire flux distribution (and the necessary number will depend greatly on solar cycle and the presence of flares and active regions), it is highly unlikely that the number of sources will increase with resolution as rapidly as the number of resolution elements.

Second, under most circumstances FASR can make use of modest frequency synthesis (combining spatial information at neighboring frequencies over a limited band) to increase the number of independent measurements in a snapshot image. It remains to be seen over what frequency range such frequency synthesis is useful, since it depends on the spectral characteristics of the emission, but it will certainly be helpful in many situations.

Third, it is always possible to spatially average (i.e. taper the beam) to reduce the resolution and decrease the number of resolution elements. So long as the number of baselines does not decrease too rapidly as the long baselines are tapered out (and indeed, the FASR array will be highly centrally condensed), FASR will retain most of its independent measurements under such tapering, and hence the image quality will improve. Thus, FASR will certainly be at least as good as NoRH, and even when heavily tapered the data will yield far more powerful diagnostics due to FASR's multi-frequency coverage.

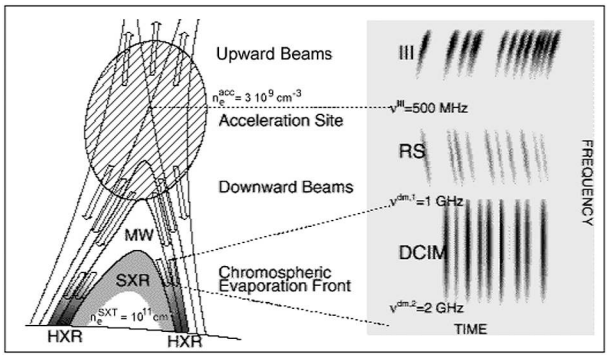

Fig. 17. Aschwanden cartoon (from Achwanden 1996).

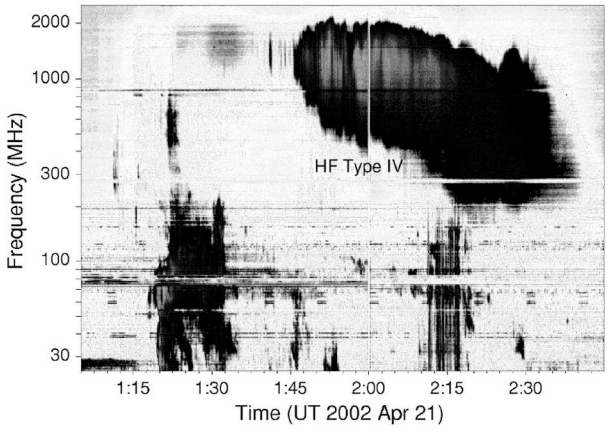

Fig. 18. Hiraiso spectrograph record showing decimetric emissions from the flare of Fig. 11 (from Kundu et al. 2004).

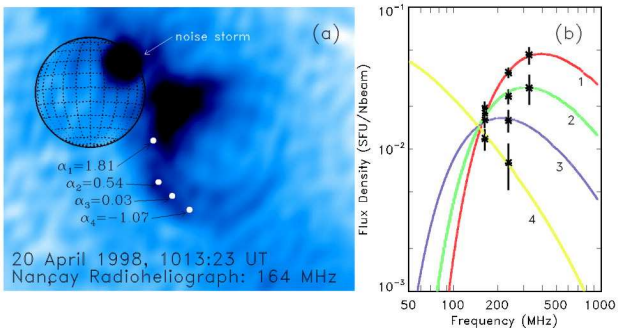

Fig. 19. CME (from Bastian et al. 2001).

4.3. How FASR Will Extend the Flare Science of NoRH

FASR's increased spatial resolution, broad spectral coverage, and improved dynamic range will yield a panoramic view of solar flares that will greatly extend the flare science that has been done to date with NoRH. In this regard, FASR is a transformative instrument—one that will transform our understanding of solar flares and many other solar phenomena through its complete coverage of solar radio emission.

As a simple example of the importance of frequency coverage, the NoRH images given in Fig. 11 (Kundu et al. 2004) were used in conjunction with RHESSI hard X-ray images to understand the initiation and subsequent development of post-flare loops of this long-duration event. However, the standard model for such long-duration events (the CSHKP model; Carmichael 1964; Sturrock 1966; Hirayama 1974; Kopp & Pneuman 1976) involves a 3D structure that is much more extended than that seen at 17 and 34 GHz. Figure 17 schematically shows some of this extended structure, emphasizing that the acceleration may take place above the newly closed loops that make up the main microwave (MW) loop (although other models such as interacting loops may apply to some bursts). Direct signatures of this acceleration may take the form of type III-like forward and reverse slope (RS) bursts as seen on a spectrograph record (right side of Fig. 17). If one wishes to have a complete picture of the relevant structure, one must obtain images in the relevant frequency range, which typically is the decimetric range (roughly 0.3-1 GHz).

That such signatures are present in the flare of Fig. 11 is amply shown in the Hiraiso spectrograph record for this event (Figure 18), as presented by Kundu et al. (2004). All of this complex radio emission is completely missed by NoRH, yet certainly can be expected to contain important clues about the extent and course of development of the 3D structure of the event.

For the first time, FASR will routinely image both the high-frequency part of the flare that NoRH sees, and the decimetric part of the event pertaining to the upper part of the 3D structure where, if the models are correct, all of the real action is. In fact, FASR will image virtually the entire range of heights shown in Fig. 17 relevant to the early stage of the events, and provide spectral diagnostics that will allow the physical parameters to be deduced throughout the region.

In at least some events, such as the one shown in Figure 19 by Bastian et al. (2001), even the accompanying coronal mass ejection (CME) may be imaged by FASR. The event in Fig. 19*a* was imaged at three frequencies by the Nançay Radioheliograph, allowing some crude spectral diagnostics (Fig. 19*b*) to be performed. The emission in this case is gyrosynchrotron emission produced by a relatively small number of energetic electrons, so constraints on the magnetic field strength and number of particles were obtained. FASR's better image quality, dynamic range, and spectral coverage will provide far better diagnostics of CMEs in their nascent stages.

5. Conclusions

The foregoing has only touched on the many discoveries made by a large number of researchers using NoRH flare data, together with supporting data from spacecraft and other groundbased observatories. The power of NoRH for flare research lies in large part on its solar-dedicated, solar-specific design, its full-Sun coverage, its imaging characteristics, and its pipelined data processing. The NoRH results, which are still being added to as more research

continues, form a legacy for flare science that is of great importance in design choices that future instruments will make, FASR in particular.

NoRH flare research has amply demonstrated that flare models need more sophistication, especially in our understanding of the importance of non-isotropic pitch-angle distributions of the accelerated particles. We can expect that the more complete frequency coverage and higher spatial resolution of FASR will clarify the fundamental relationships between the small-scale, lower-atmosphere phenomena and the large-scale phenomena of importance to space weather, which the NoRH observations have hinted at.

With FASR, solar radio physics is poised for the next great step, a transformative leap to a new understanding for all of solar and space weather physics. FASR will succeed only when we fully heed the legacy of the NoRH.

Acknowledgments: This work was supported by NSF grant AST-0307670 to New Jersey Institute of Technology. The author gratefully acknowledges financial support from the organizers of the Nobeyama symposium to attend the meeting.

References

Altyntsev, A. T., Grechnev, V. V., Nakajima, H., Fujiki, K., Nishio, M. & Prosovetsky, D. V. 1999, A&AS, 135, 415

Asai, A., Shimojo, M., Isobe, H., Morimoto, T., Yokoyama, T., Shibasaki, K. & Nakajima, H. 2001, ApJL, 562, L103

Aschwanden, M. J. 1996, American Institute of Physics Conference Series, 374, 300

Aurass, H., Shibasaki, K., Reiner, M. & Karlický, M. 2002, ApJ, 567, 610

Bastian, T. S. 1994, ApJ, 426, 774

Bastian, T. S. 1999, Proceedings of the Nobeyama Symposium, held in Kiyosato, Japan, Oct. 27-30, 1998, Eds.: T. S. Bastian, N. Gopalswamy and K. Shibasaki, NRO Report No. 479., 211

Bastian, T. S., Pick, M., Kerdraon, A., Maia, D., & Vourlidas, A. 2001, ApJL, 558, L65

Bastian, T. S. 2003*a*, Proc. SPIE, 4853, 98

Bastian, T. S. 2003*b*, Adv. in Space Res., 32, 2705

Carmichael, H. 1964, in Proc. NASA Symp. on the Physics of Solar Flares, ed. W. N. Hess (NASA SP-50), 451

Gary, D. E. 2003, J. Korean Astr. Soc., 36, 135

Gary, D. E., Hartl, M. D., Shimizu, T. 1997, ApJ477, 958

Gary, D. E. & Keller, C. U. 2003, Proc. SPIE, 4853, 523

Gary, D. E., & Keller, C. U. 2004, Solar and Space Weather Radiophysics—Current Status and Future Developments. Edited by Dale E. Gary & Christoph U. Keller, ASTROPHYSICS AND SPACE SCIENCE LIBRARY Volume 314 Kluwer Academic Publishers, Dordrecht, 400pp

Grechnev, V. V. White, S. M. & Kundu, M. R. 2003, ApJ, 588, 1163

Hanaoka, Y. 1997, Sol. Phys., 173, 319

Hanaoka, Y. 1999, PASJ, 51, 483

Hirayama, T. 1974, Sol. Phys., 34, 323

Hori, K., Kosugi, T., Fujiki, K., Koshiishi, H., & Shibasaki, K. 2000, ApJ, 533, 557

Kopp, R. A., & Pneuman, G. W. 1976, Sol. Phys., 50, 85

Kundu, M. R., Nitta, N., White, S. M., Shibasaki, K., Enome, S., Sakao, T., Kosugi, T., & Sakurai, T. 1995, ApJ, 454, 522

Kundu, M. R., White, S. M., Shibasaki, K., & Sakurai, T. 2000, ApJ, 545, 1084

Kundu, M. R., White, S. M., Shibasaki, K., Sakurai, T., & Grechnev, V. V. 2001*a*, ApJ, 547, 1090

Kundu, M. R., White, S. M., Shibasaki, K., & Raulin, J.-P. 2001*b*, ApJS, 133, 467

Kundu, M. R., Nindos, A., White, S. M., & Grechnev, V. V. 2001*c*, ApJ, 557, 880

Kundu, M. R., Garaimov, V. I., White, S. M., & Krucker, S. 2004, ApJ, 600, 1052

Lee, J., Gary, D. E., & Shibasaki, K. 2000, ApJ, 531, 1109

Lin, R. P., Schwartz, R. A., Kane, S. R., Peling, R. M. & Hurley, K. C. 1984, ApJ, 283, 421

Melnikov, V. F., Shibasaki, K., & Reznikova, V. E. 2002*a*, ApJL, 580, L185

Melnikov, V. F., Reznikova, V. E., Yokoyama, T., & Shibasaki, K. 2002*b*, ESA SP-506: Solar Variability: From Core to Outer Frontiers, 339

Nakajima, H., et al. 1994, Proc. IEEE, 82, 705

Nakajima, H., & Yokoyama, T. 2002, ApJL, 570, L41

Nishio, M., Yaji, K., Kosugi, T., Nakajima, H., & Sakurai, T. 1997, ApJ, 489, 976

Nishio, M., Kosugi, T., Yaji, K., Nakajima, H., & Sakurai, T. 2000, Advances in Space Research, 25, 1791

Raulin, J.-P., White, S. M., Kundu, M. R., Silva, A. V. R., & Shibasaki, K. 1999, ApJ, 522, 547

Shibasaki, K., et al. 1994, Space Science Reviews, 68, 217

Shibasaki, K. 2002, ApJL, 567, L85

Sturrock, P. A. 1966, Nature, 211, 695

White, S. M., Kundu, M. R., Shimizu, T., Shibasaki, K., & Enome, S. 1995, ApJ, 450, 435

White, S. M., Kundu, M. R., Garaimov, V. I., Yokoyama, T., & Sato, J. 2002, ApJ, 576, 505

White, S. M., Lee, J., Aschwanden, M. A. & Bastian, T. S. 2003, Proc. SPIE, 4853, 531

Yokoyama, T., Nakajima, H., Shibasaki, K., Melnikov, V. F., & Stepanov, A. V. 2002, ApJL, 576, L87

Yokoyama, T., Nakajima, H., Shibasaki, K., Melnikov, V. F., & Stepanov, A. V. 2003, Advances in Space Research, 32, 2517